HHS Public Access

Author manuscript

Magn Reson Med. Author manuscript; available in PMC 2018 January 01.

Published in final edited form as:

Magn Reson Med. 2017 January ; 77(1): 434–443. doi:10.1002/mrm.26487.

Towards imaging the body at 10.5 tesla

M. Arcan Ertürk[1], **Xiaoping Wu**[1], **Yiğitcan Eryaman**[1], **Pierre-François Van de Moortele**[1], **Edward J. Auerbach**[1], **Russell L. Lagore**[1], **Lance DelaBarre**[1], **J. Thomas Vaughan**[1,2], **Kâmil Uğurbil**[1], **Gregor Adriany**[1], and **Gregory J. Metzger**[1]

[1]Center for Magnetic Resonance Research, University of Minnesota, Minneapolis, Minnesota, United States

[2]Department of Biomedical Engineering in The Mortimer B. Zuckerman Mind Brain Behavior Institute, Columbia University, New York, United States

Abstract

Purpose—To explore the potential of performing body imaging at 10.5T compared to 7.0T through evaluating the transmit/receive performance of similarly configured dipole antenna arrays.

Methods—Fractionated dipole antenna elements for 10.5T body imaging were designed and evaluated using numerical simulations. Transmit performance of antenna arrays inside the prostate, kidneys and heart were investigated and compared to those at 7.0T using both phase-only RF shimming and multi-spoke pulses. Signal-to-noise ratio (SNR) comparisons were also performed. A 10-channel antenna array was constructed to image the abdomen of a swine at 10.5T. Numerical methods were validated with phantom studies at both field strengths.

Results—Similar power efficiencies were observed inside target organs with phase-only shimming, but RF non-uniformity was significantly higher at 10.5T. Spokes RF pulses allowed similar transmit performance with accompanying local SAR increases of 25–90% compared to 7.0T. Relative SNR gains inside the target anatomies were calculated to be >2-fold higher at 10.5T, and 2.2-fold SNR gain was measured in a phantom. Gradient echo and fast spin echo imaging demonstrated the feasibility of body imaging at 10.5T with the designed array.

Conclusion—While comparable power efficiencies can be achieved using dipole antenna arrays with static shimming at 10.5T; increasing RF non-uniformities underscore the need for efficient, robust and safe parallel transmission methods.

Keywords

10.5 tesla; body imaging; body imaging at ultra-high field; dipole antenna; parallel transmission

Corresponding Author: M. Arcan Ertürk, PhD, Center for Magnetic Resonance Research, University of Minnesota Medical School, 2021 6th Street SE, Minneapolis, MN 55455, arcan@umn.edu.

Part of this work was presented at the 24th Annual Meeting & Exhibition of ISMRM (abstract #390).

INTRODUCTION

Moving to higher static magnetic field strengths (B_0) can increase the sensitivity of magnetic resonance (MR) studies, improve susceptibility contrast and increase chemical shift dispersion. Since the inception of MRI, pushing toward higher field strengths to seek answers to physiological and biological questions has been the goal of many researchers. Currently, approximately 60 ultra-high field (UHF, $B_0 \geq 7.0$ tesla (7.0T)) human scanners are in operation world-wide with a majority of them being 7.0T systems (1). A number of systems that are beyond 10T are being planned or have been installed (2). Notably, the first whole-body 10.5T human scanner has recently been ramped to field and is operational. However, with the increasing field strength, electro-magnetic (EM) wavelengths inside the tissues become shorter, causing destructive transmit B_1 (B_1^+) interferences. In addition, local specific absorption rate (SAR) increases with the field strength, a constant concern at UHF. Tackling these challenges via radiofrequency (RF) coil designs and parallel transmission (pTx) methods is an active area of research, which has shown potential for imaging several target anatomies inside the body at 7.0T (3,4).

Arrays of dipole antennae have been used increasingly for body imaging at 7.0T because of their favorable field distributions, increased power efficiency at depth and improved SAR performance (5–8). Current distribution on the coil element plays an important role in shaping the EM fields inside the so-called “near field” region; however at larger depths (i.e. outside the near-field region) where propagating EM waves become more dominant, wave propagation effects need to be considered for optimal coil design. It has been shown at 7.0T that outside the “near-field” regime, antenna elements (e.g., dipole antennae) allowing high wave propagation directivity may provide improved B_1^+ efficiency inside the body compared to conventional coil elements (e.g., microstrip line and loop coil elements) (8,9). Because the near-field region is pushed closer to the element at 10.5T compared to 7.0T, dipole antenna elements are anticipated to have a better performance than the microstrip line and resonating loop elements for most body imaging applications.

Solely from the transmit RF management perspective, imaging the body is expected to be more challenging at 10.5T than at 7.0T, because wavelengths inside the tissue are reduced to around 9 cm. The goal of this work was to determine the main differences and major challenges for 10.5T body imaging by comparing local transceiver arrays of similar configurations to those at 7.0T. Specifically, we designed fractionated dipole antenna elements for body imaging at 10.5T using a similar methodology reported by Raaijmakers et al (10). These individual elements were used to simulate a 10-channel array for which transmit performance (i.e. power efficiency, field uniformity and RF safety) as well as receive performances inside the prostate, kidneys and heart were investigated and compared to a similar design at 7.0T. To validate the electromagnetic modeling results, the 10-channel dipole array was constructed for 10.5T and used to experimentally obtain transmit B_1^+ and SNR measurements for comparison with similarly obtained 7.0T data in a uniform torso-sized saline phantom. Finally, MRI of the abdomen of a large swine was obtained to demonstrate the feasibility of performing body imaging studies at 447 MHz.

METHODS

Design of a fractionated dipole antenna element for 10.5 tesla

Fractionated dipole antenna elements at 10.5T were designed (10) using a finite-difference time-domain (FDTD) solver (SEMCAD X software V14.8, SPEAG, Zürich, Switzerland), for a proton Larmor frequency of 447 MHz. The dipole antenna was placed 2 cm away from the surface of a uniform rectangular phantom (dimensions: 20×20×40 cm^3) of which the electrical properties mimic the human body ($\varepsilon_r = 36$, $\sigma = 0.42$ S/m). The basic fractionated dipole element structure used in this work consists of two arms, with each arm sectioned at two locations (Figure 1.a) where the neighboring sections on each arm are connected with identical reactive components. Our design procedure was as follows: first an approximate total length of the dipole element was determined. This was accomplished by simulating EM-field distributions inside the phantom for a range of element lengths (between 18 and 30 cm). The resulting peak 10g averaged local SAR (SAR_{10g}) was calculated followed by the calculation of power efficiency (i.e., $B_1^+/W^{0.5}$) and SAR efficiency (i.e., $B_1^+/SAR_{10g}{}^{0.5}$) inside 8 cm^3 cubes located at depths of 4, 6, 8 and 10 cm. The goal was to determine a length which gave high power efficiency at depths greater than 8 cm. After the length was found, the value of the reactive components was determined. For this, another set of simulations were performed for a range of reactance values (between −60Ω (i.e. capacitive) and 120Ω (i.e. inductive)). The goal was to achieve reactance values that yielded both favorable power and SAR efficiencies at depths of 8 cm and deeper.

Comparison of 7.0 and 10.5 tesla dipole antennae elements

Peak local SAR and power efficiency distributions of dipole antenna elements at 10.5T were compared against fractionated dipole antenna elements previously developed by Raaijmakers et al. at 7.0T (10). Simulations were performed using an FDTD solver with the same phantom used for element length evaluations. Additionally, in each case two dipole antenna elements were placed next to each other on the rectangular phantom. Mutual coupling as a function of inter-element distance was calculated by varying the center-to-center distance between the two elements from 4 to 10 cm with 1 cm increments.

Numerical analysis of 10-channel antenna arrays on an anatomical human model

Array performances of the 7.0T and 10.5T dipole elements were investigated inside the prostate, kidneys and heart of an adult male human model (“Duke” from Virtual Family v1.0) (11) at 297.2 and 447 MHz, respectively. Ten antenna elements were placed around the pelvis, abdomen and chest of Duke for the prostate, kidney and heart simulations, respectively. A total of six simulations were performed (prostate, kidney and heart simulation locations; 7.0 and 10.5T ^{1}H Larmor frequencies) using correct frequency specific electrical properties (12). Conductors of the antenna elements were 2 cm away from the tissue surface and were placed at geometrically identical locations both at 7.0 and 10.5T. All elements were terminated with 50Ω voltage source ports. The entire body and the gradient shield were included in the simulations. EM-field distributions of each antenna element were computed using an FDTD solver. EM field solutions inside Duke within a 30 cm-long region centered at the antenna elements along the z-dimension were extracted. Meshing resolution within the antenna conductors and inside the 30 cm-long region where the EM-fields were

extracted was ≤1 mm. The mesh resolution of the simulation was gradually coarsened outside the region of interest to accelerate computations. Mesh sizes ranged between 100–133 Million cells (120.9±12.4 Million cells). EM-field distributions were imported to MATLAB (Mathworks, Natick, Massachusetts) for post processing and analysis.

EM-field distributions were re-gridded onto a uniform 2 mm grid using nearest-neighbor interpolation. SAR Q-matrices were formed using a modified version of the N-gram averaging algorithm developed by Carluccio et al. (13). The SAR Q-matrices were further compressed into a largely reduced number of virtual observation points (VOPs) (14) which were subsequently used for pTx spoke pulse design to accelerate the estimation of peak 10g-averaged local SAR. The SAR overestimation percentage used in creating the VOPs was 5% for 10.5T and 10% for 7.0T simulations, yielding comparable absolute overestimation at both field strengths for a given target organ.

Power efficiency, field uniformity, peak local SAR and SAR efficiency metrics were used to assess the transmit performance of the antenna arrays at both field strengths targeting the prostate, kidneys and heart. Field uniformity was quantified using the coefficient of variation (CV; i.e., SD/mean) of B_1^+ inside each target organ (i.e. prostate, kidneys, or heart). A range of phase-only shim solutions were calculated by varying the tradeoff between power efficiency and field uniformity.

Relative SNR values of the antenna arrays were numerically calculated by combining the normalized receive B_1 (B_1^-) distributions of individual antenna elements in a root sum-of-squares (RSOS) fashion and scaling with the square of B_0 to account for the field-strength related increase in signal power (15):

$$\mathrm{SNR}_{\mathrm{relative}} \sim \left(\frac{B_0}{7.0}\right)^2 \cdot \sqrt{\sum_{n=1}^{10}\left(\frac{|B_{1,n}^-|}{\sqrt{P_n}}\right)^2} \quad [1]$$

where B_0 is the field strength, $\frac{|B_{1,n}^-|}{\sqrt{P_n}}$ is the magnitude of the receive B_1 field normalized to 1 W of accepted power for the n^{th} antenna element.

Parallel transmission using spoke pulses

In addition to phase-only RF shimming as is typically performed at 7.0T, we designed pTx spoke pulses (16) to evaluate the performances of the 10-channel dipole arrays at 7.0T and 10.5T when exploiting parallel transmit capabilities. For each target organ (i.e., prostate, kidneys and heart), single- and 2-spoke pTx pulses were designed for slab-selective excitation targeting a uniform flip angle (FA) distribution within the region of interest (ROI) and were designed with an explicit local SAR constraint. The design problem was formulated in the image domain (17) as a constrained minimization (18,19) to seek channel-specific and spoke-specific RF weights (i.e., magnitude and phase modulations) that minimize the excitation error while satisfying a predefined local SAR limit. The excitation

error was quantified in the magnitude least squares sense (20) assuming small tip angle excitation, and the peak 10 g SAR estimated by using VOPs.

To improve RF performance in the 2-spoke pulse design, the spoke positioning in the excitation k-space was determined by an additional optimization process. To have an equivalent but reduced parameter space, the first spoke was always positioned at the origin of the excitation k-space and only the placement of the second spoke was variable (21). The placement of the second spoke was tuned by an exhaustive search over a large number of candidate placements. Instead of a 2D grid restricted to the kx-ky plane, the candidate placements were predefined on a 3D grid of the excitation k-space. This was done to increase the degrees of freedom in pulse design, thereby producing more homogeneous flip angles in a 3D ROI. The gridding of the k-space was based on spherical coordinates (i.e., kr, kθ, kφ). The radius (kr) was incremented from 1/FOV to 3/FOV in steps of 0.2/FOV where FOV is the average dimension of the target organ, while the polar (kθ) and azimuthal (kφ) angles were both incremented from 0° to 180° in steps of 45°. The placement that minimized the Tikhonov regularized least squares was chosen as the best location of the second spoke and was used for the subsequent local SAR constrained 2-spoke pulse design. The resulting 3D gradient blips were similar to those associated with kT point pulses (22) which have been shown to be effective for volumetric flip angle homogenization.

In all cases, the constrained minimization pulse design was solved using “fmincon” in Matlab for which the initial point was obtained by solving a least square minimization with Tikhonov regularization (17). For all pulse designs, the nominal flip angle was set to 45 degrees where the sub-pulses consisted of a sinc waveform with a time bandwidth product of 4 and a pulse length of 1 ms. Furthermore, the local SAR was evaluated assuming a duty cycle of 10% for single-spoke and 20% for 2-spoke pulse designs.

To characterize the RF performance of the dipole arrays, the L-curve demonstrating the tradeoff between excitation fidelity and the resulting local SAR was obtained by varying the predefined local SAR limits during pulse design. Specifically, the predefined local SAR limit was varied from 1 to 20 W/kg for investigated anatomies. The excitation fidelity was evaluated using normalized root mean square error (NRMSE) of the excitation which quantifies the deviation of the resulting flip angles within the target organ from the nominal flip angles. The local SAR was calculated using the SAR Q-matrices, not the VOP’s which were only used during pulse design. In addition, the average forward total antenna array power for duty cycles of 10% and 20% were calculated for 1- and 2-spoke pulse designs, respectively. Average flip angle values inside the investigated organs were computed for the designed spoke pulses.

Implementation of 10.5 T 10-channel dipole antenna array

In order to conduct experimental studies in phantoms and in vivo, a 10-channel dipole antenna array was constructed matching that modeled in simulations. The elements of this array were etched on double-sided FR4 printed circuit boards (PCBs) (Figure 1.b). PCBs were mounted between two 9.5 mm-thick thermoplastic polyehterimide blocks (ULTEM 1000 resin, Sabic Global, Pittsfield, Massachusetts). Dipole antenna elements were initially fine-tuned on a human body at 447 MHz by adjusting their lengths and matched to better

than −15 dB using first-order lattice balun networks. Two flexible fabric housings (anterior and posterior) were used to place the antenna elements around the object being imaged while maintaining a center-to-center separation of ~9 cm between neighboring elements (Figure 1.c), with the anterior housing containing 6 and the posterior housing 4 antenna elements. The 9 cm spacing was initially used to match the geometry of the 7.0T array used in previous work (10).

10.5 T MRI system properties and experimental methods

MRI experiments were conducted on a whole-body 10.5 tesla scanner (Siemens Healthcare, Erlangen, Germany), equipped with 32 receive and 16 transmit channels. Each transmit channel was driven by 2-kW power amplifiers (Stolberg HF-Technik AG, Stolberg, Germany). The 10-channel transceiver dipole antenna array was interfaced to the scanner via a 16-channel transmit/receive box (Virtumed LLC, Minneapolis, Minnesota).

Phantom validation studies

To validate numerical computations, matching experiments and simulations were performed using an ~18L torso-sized phantom (23) filled with a saline solution (4.5 g/l NaCl, 1 g/l $CuSO_4$), with electrical properties (ε_r = 77.8, σ = 0.82 S/m) and (ε_r = 77.5, σ = 0.85 S/m) at 7.0 and 10.5 tesla ^{1}H Larmor frequencies, respectively. Experiments were conducted on 7.0T and 10.5T whole-body scanners (Siemens Healthcare, Erlangen, Germany) with identical data acquisition protocols. Flip angle maps were acquired with the actual flip angle technique (24) (TR_1/TR_2/TE: 20/120/3 ms; nominal FA = 50°; voxel-size: 2×2×4 mm^3; acquisition matrix: 226×226×64) and were used to calculate power efficiency distributions. SNR data were acquired using a fully-relaxed GRE sequence (TR/TE: 10000/3.1 ms; FA = 90°; voxel-size: 2×2×8 mm^3; acquisition matrix: 226×226×32) followed by a noise scan with minimum TR and no RF excitation (25).

First, power efficiency distributions of single dipole antenna elements inside the phantom were measured at both field strengths, and matching simulations were performed at both ^{1}H Larmor frequencies. Power losses in the transmit chain (i.e. T/R switch, cable and mismatch losses) were measured and accounted for. In addition, B_1^+ and SNR distributions of the 10-channel dipole antenna arrays were investigated on the torso phantom at both field strengths, with six elements placed anteriorly and four elements posteriorly. Phase-only efficiency shimming inside a 24×24 mm^2 square region approximating the size and location of the prostate was performed (26). Power efficiency and SNR distributions were calculated both experimentally and numerically with simulations closely matching experimental conditions. Power efficiency and SNR ratios between 7.0 and 10.5 tesla arrays were calculated inside centrally located cubes (24 mm edge length) and compared with experimental results to assess the accuracy of numerical simulations. Furthermore, SNR gains inside a 24×24 mm^2 square region were calculated for each slice to investigate the extent of SNR gains along the z-dimension of the phantom.

Imaging studies

To demonstrate the potential for imaging the body at 10.5T, the 10 channel dipole array was used to obtain renal images of a 75 kg female swine post-mortem (19 cm in the anterior-

posterior dimension). To improve RF efficiency and uniformity, phase-only RF shimming targeting both kidneys was conducted prior to the anatomical image acquisitions. Both 3D gradient echo (GRE) and multi-slice fast spin-echo (FSE) images were acquired. The 3D GRE images were acquired in axial and coronal views with TR/TE = 17/2.7 ms, voxel-size = 1.2×1.2×3 mm^3, FOV = 460×460×96 mm^3, and total duration = 5m 14s. The multi-slice FSE image was acquired in the coronal view with TR/TE = 4000/42 ms, voxel-size = 1.8×1.8×3 mm^3, FOV = 450×450×21 mm^3, and duration = 1m 52s.

RESULTS

Design of a fractionated dipole antenna at 10.5 tesla

A dipole antenna length of 22 cm was identified as providing high power efficiency at depths greater than 8 cm inside the phantom compared to other investigated antenna lengths. Inductive reactance values along antenna arms tended to decrease local SAR efficiency and power efficiency close to the elements (i.e. depths <5 cm), but demonstrated improved SAR efficiency at depths greater than 8 cm. Therefore, a reactance value of ~25Ω was chosen, which is a trade-off between power and SAR efficiencies at depths greater than 8 cm. Increasing the inductance value further could significantly reduce the power efficiency of the dipole antenna. The chosen inductance value was realized by two 24 mm-wide meanders on each arm (Figure 1.b). Because of the variations between simulated and experimental loading conditions, the physically implemented dipole antenna elements were shortened to 21 cm to achieve resonance at 447 MHz.

Power efficiency distributions for 7.0T and 10.5T dipole antenna elements inside a uniform phantom along axial and sagittal slices are shown in Figure 2. Due to its shorter length, the full-width half-maximum (FWHM) of power efficiency for the 10.5T antenna along the z-dimension was 28% shorter than that of 7.0T, resulting in reduced coverage at 10.5T in that dimension. The power efficiency of the 10.5T antenna was 27% and 17% higher at depths of 4 and 10 cm, respectively, with 76% higher peak 10g SAR than the 7.0T antenna.

Mutual coupling between two antenna elements at various center-to-center distances are plotted in Figure 3. At a distance of 80 mm, coupling between antenna elements was −12.6 and −16.5 dB at 7.0T and 10.5T, respectively. For a target decoupling value of ≤−12 dB, 7.0T and 10.5T antenna elements could be placed at center-to-center distances of ≥ 80 and 60 mm, respectively.

Numerical comparison of 7.0 and 10.5 T dipole antenna arrays for imaging the body

The plot of numerically computed power efficiency versus coefficient of variation (CV) inside the prostate with phase-only shimming (Figure 4.a) demonstrates that both antenna arrays can provide similar power efficiencies at their respective field strengths, however the resulting field uniformity at 7.0T is superior. Using a phase-only shim solution optimized for power efficiency at 10.5T, 133% higher CV was observed compared to an efficiency shim solution at 7.0T (Supporting Figure S1.a–b). A phase-only shim solution optimized for field uniformity at 10.5T, yielded 79% higher CV than an efficiency solution at 7.0T. SAR efficiency inside the prostate and peak 10g local SAR of the arrays are plotted in Figure 4.b,

showing that the 7.0T antenna array can achieve slightly lower (~10%) SAR levels compared to 10.5T inside the prostate. Power efficiency vs CV distributions inside the kidneys and heart are plotted in Figure 4.c and e, respectively. In both organs, both antenna arrays provide similar power efficiency while field uniformity at 10.5T is poorer. SAR efficiency of the antenna arrays inside the kidneys and heart are plotted against peak 10g SAR in Figure 4.d and f, respectively. Peak SAR values of the 10.5T array are on average 130% and 62% higher than its 7.0T counterpart with kidney and heart specific shim solutions, respectively. Even though both arrays can provide similar power efficiencies, SAR efficiency of 10.5T array is lower inside the kidneys and heart by 35 and 23%, respectively, due to its higher local SAR deposition.

L-curves demonstrating the tradeoffs between excitation error (i.e. NRMSE) and local SAR limit for various design scenarios are plotted in Figure 5.a–c. For the same target organ and number of spokes, RF performance was worse at 10.5T where SAR increased by 25–35% for prostate, 60–80% for kidneys and 50–90% for heart when achieving comparable excitation fidelity inside the target organ. However, for kidneys and heart, designing 2-spoke pulses at 10.5T appeared to yield similar RF performance to single-spoke designs at 7.0T. For prostate, designing 2-spoke pulses at 10.5T started to outperform the single-spoke design at 7.0T. L-curves demonstrating the relation between forward antenna array power and NRMSE are shown in Figure 5.d–f. The range of average FAs achieved in the target anatomies over the range of powers applied are listed in Supporting Table S1 for the pulses designed for each target anatomy. FAs of approximately 45° are achieved at both 7.0 and 10.5T inside the prostate and kidneys, however 2-spoke pulse designs are required at 10.5T in the kidneys. Inside the heart, an average FA close to 45° is achieved only with a 2-spoke pulse at 7.0T and, given the design constraints, not achieved at 10.5T due to the local SAR limits being reached.

RSOS combination of normalized receive fields from simulation on axial slices intersecting the prostate, kidneys and heart for the antenna arrays at 7.0T and 10.5T are shown in Supporting Figure S2, and mean values are listed in Table 1. Average B_1^- performance of the antenna arrays are within ±6% of each other. Simulated relative SNR gains at 10.5T are calculated using Eq. [1], and listed in Table 1. More than two-fold gains are anticipated at 10.5T in all imaging targets under investigation using dipole antenna arrays with the same number of channels, while excluding the field strength dependent spin relaxation effects.

Phantom validation studies

Power efficiency distributions of dipole antenna elements inside the torso phantom along an axial slice intersecting the center of the elements are shown in Supporting Figure S3; with top and bottom rows depicting numerical and experimental results, respectively. Power efficiency profiles of the elements are plotted in Supporting Figure S3.c and f, respectively demonstrating good agreement between simulations and experiments. Power efficiency and SNR distributions of the 10-channel dipole antenna arrays are shown in Supporting Figure S4 and Supporting Figure S5, respectively. Top and bottom rows show numerical and experimental results, respectively; while left and right columns demonstrate the SNR distributions at 7.0T and 10.5T, respectively. Measured SNR maps fail to provide accurate

results in regions of low power efficiency with the chosen shim solutions, and results are reported from inside the annotated regions where reliable RF excitation is generated. Simulated and measured power efficiency ratios for 7.0T and 10.5T inside annotated cubes are 1.00 and 1.04, respectively. SNR gains at 10.5T are 2.39- and 2.26-fold inside annotated regions from simulation and experiment, respectively. Numerical and experimental results are within 6% of each other with respect to the power efficiency and SNR investigations of the 10 channel antenna array, validating the accuracy of EM-field simulations. The 10.5T dipole antenna array provides SNR gains of >2.25-, >2- and >1.5-fold when looking at larger extents along the z-dimension of 58, 110 and 200 mm, respectively (Supporting Figure S6).

Imaging studies

Anatomical axial and coronal GRE images inside the abdomen of a swine are shown in Figure 6.a–b, respectively, with phase-only RF shimming providing acceptable field transmission inside the kidneys. Coincidently, renal cysts were observed in the swine imaged in these studies. Coronal FSE images (Figure 6.c) show improved contrast between the cystic lesion and normal appearing renal anatomy compared to respective GRE images. In the FSE images, parts of the renal tissues and borders of the kidneys towards the middle of the coronal imaging slices were not visible due to B_1^+ dropout in those locations.

DISCUSSION

We designed dipole antenna elements for imaging the body at 10.5T using a similar methodology to the one described by Raaijmakers et al (10). An array of the new elements was then compared against a similar antenna array configuration at 7.0T (10). Due to the higher Larmor frequency at 10.5T, optimized dipole antenna element lengths were shorter than similarly designed 7.0T counterparts, yielding a reduced coverage in the z-dimension. The coverage of the 10.5T antenna array was suitable for prostate imaging, however renal and cardiac imaging would benefit from coverage similar to that provided by the 7.0T array. A larger imaging FOV along z could be supported by using longer antennae with capacitive loading, by interleaving the elements along z-dimension and/or placing elements in mulitple rows (27–30). In this work, we used a similar antenna design methodology at 10.5T to that originally used for 7.0T, kept the number of antenna elements the same and placed them at identical locations at both field strengths and in all imaging locations (i.e. around the pelvis, abdomen and chest of Duke) in order to minimize the number of variables between field strengths.

Coupling between neighboring antenna elements at a given separation is lower at 10.5T, which may enable development of arrays with higher element densities and channel counts (31). Reduction in mutual coupling can be explained by the increased EM field phase variation and shortened wavelength at higher frequencies (31). Even though not explicitly investigated in this work, larger spatial phase variations at higher frequencies results in more distinct individual coil sensitivity profiles and improved parallel imaging performance at higher field strengths (32). Element count and density can also be increased by shortening the length of the antennae by using high permittivity blocks (7), by further distributing the

inductance along the arms of the antenna (33,34) and by combining antenna elements with loop coils (35,36). Development and evaluation of an improved 10.5T body imaging array with higher number of channels will be the focus of future work.

Our results show that dipole antenna arrays have similar power efficiencies and peak local SAR with phase-only shimming inside the prostate, however with increased frequency and decreased wavelength, field uniformity was significantly worse at 10.5T. The SAR increase observed when achieving similar excitation errors (i.e. NRMSE) inside the investigated target organs ranged between 25 and 90%, lower than the quadratic SAR relation to B_0 (37) (i.e. 125% at 10.5T vs 7.0T), and in agreement with more recent work investigating electrodynamic constraints at higher frequencies (31,38,39).

Quadratic SNR gains with increasing B_0 were previously observed with minimally invasive monopole antennae at 3.0T and above (40,41), and here again quadratic SNR gains at 10.5T are anticipated against 7.0T in numerical simulations (i.e. ~125%, Table 1) and also measured in saline phantoms (Supporting Figure S5). It is worth noting that the smaller coverage of the 10.5T array along the z-dimension biases SNR comparisons by limiting the noise contribution from tissues outside the region of interest, especially in smaller imaging targets such as the prostate and kidneys. If the coverage of the coils were the same at both field strengths while keeping the number of elements unchanged, a more moderate supra-linear SNR gain recently reported by Pohmann et al. may be expected (42). However, dense receiver arrays as used in this previous work, are not currently available for UHF body imaging, and will need to be developed in order to realize the potential gains in SNR. Similarly, the shorter z-coverage of the 10.5T array is favorable for imaging the prostate, yielding up to 35% higher peak SAR compared to 7.0T while achieving similar transmit performance. In contrast, up to 90% more peak SAR is observed for similar transmit performance in larger organs (i.e. heart). These results underscore the importance of target specific array optimization at UHF.

In vivo studies in healthy human subjects at 10.5T will be conducted upon receiving the U.S. Food and Drug Administration (FDA) and institutional review board approvals. In the absence of running human volunteers, large swine were imaged at 10.5T post-mortem. Imaging of a live swine was not pursued because post-mortem imaging was deemed satisfactory to evaluate the EM-field behavior *in vivo*. RF transmit performance was sufficient to obtain acceptable image quality inside the kidneys of a swine using GRE sequences. However, achieving the desired transmit performance when performing RF pulse sequences with high levels of power deposition (i.e. FSE) at 10.5T may not be accomplished using static (26,43,44) or dynamically applied static RF shimming methods (45) inside medium- and large-sized targets. Several RF management strategies such as RF excitation using time-interleaved acquisition of modes (46), multi-spoke pulses (22,47), pTx RF pulse design (48–52), or direct signal control approaches (53–55) may be employed to overcome some of the challenges. Furthermore, incorporation of novel quantitative imaging methods that can perform in the presence of heterogeneous RF fields may alleviate the need of strict transmit field control (56). Numerical modeling, validation and real-time monitoring of RF safety (57–64) will play an important role in successful implementation of pTx methods. Even though increasing B0 and Larmor frequency poses challenges in terms of field

uniformity and RF management, it also opens up new opportunities for transmit array design using higher element densities and channel counts.

Supplementary Material

Refer to Web version on PubMed Central for supplementary material.

Acknowledgments

Supported by: NCI R01 CA155268, WM Keck Foundation, NIBIB P41 EB015894.

We thank Alexander Raaijmakers (Utrecht Medical Center) for providing the design of 7.0T fractionated dipole antenna elements.

REFERENCES

1. Healthcare, S. Siemens MAGNETOM Terra Product Brochure. Erlangen, Germany: Siemens Healthcare GMBH; 2015. p. 53
2. Budinger TF, Bird MD, Frydman L, Long JR, Mareci TH, Rooney WD, Rosen B, Schenck JF, Schepkin VD, Sherry AD, Sodickson DK, Springer CS, Thulborn KR, Ugurbil K, Wald LL. Toward 20 T magnetic resonance for human brain studies: opportunities for discovery and neuroscience rationale. MAGMA. 2016
3. Kraff O, Fischer A, Nagel AM, Monninghoff C, Ladd ME. MRI at 7 Tesla and above: demonstrated and potential capabilities. J Magn Reson Imaging. 2015; 41(1):13–33. [PubMed: 24478137]
4. Padormo F, Beqiri A, Hajnal JV, Malik SJ. Parallel transmission for ultrahigh-field imaging. NMR Biomed. 2015
5. Raaijmakers AJ, Ipek O, Klomp DW, Possanzini C, Harvey PR, Lagendijk JJ, van den Berg CA. Design of a radiative surface coil array element at 7 T: the single-side adapted dipole antenna. Magn Reson Med. 2011; 66(5):1488–1497. [PubMed: 21630342]
6. Duan Q, Nair G, Gudino N, de Zwart JA, van Gelderen P, Murphy-Boesch J, Reich DS, Duyn JH, Merkle H. A 7.0T spine array based on electric dipole transmitters. Magn Reson Med. 2015; 74(4): 1189–1197. [PubMed: 26190585]
7. Oezerdem C, Winter L, Graessl A, Paul K, Els A, Weinberger O, Rieger J, Kuehne A, Dieringer M, Hezel F, Voit D, Frahm J, Niendorf T. 16-channel bow tie antenna transceiver array for cardiac MR at 7.0 tesla. Magn Reson Med. 2016; 75(6):2553–2565. [PubMed: 26183320]
8. Raaijmakers AJ, Luijten PR, van den Berg CA. Dipole antennas for ultrahigh-field body imaging: a comparison with loop coils. NMR Biomed. 2015
9. Ipek O, Raaijmakers AJ, Klomp DW, Lagendijk JJ, Luijten PR, van den Berg CA. Characterization of transceive surface element designs for 7 tesla magnetic resonance imaging of the prostate: radiative antenna and microstrip. Phys Med Biol. 2012; 57(2):343–355. [PubMed: 22170777]
10. Raaijmakers AJ, Italiaander M, Voogt IJ, Luijten PR, Hoogduin JM, Klomp DW, van den Berg CA. The fractionated dipole antenna: A new antenna for body imaging at 7 Tesla. Magn Reson Med. 2016; 75(3):1366–1374. [PubMed: 25939890]
11. Christ A, Kainz W, Hahn EG, Honegger K, Zefferer M, Neufeld E, Rascher W, Janka R, Bautz W, Chen J, Kiefer B, Schmitt P, Hollenbach HP, Shen J, Oberle M, Szczerba D, Kam A, Guag JW, Kuster N. The Virtual Family--development of surface-based anatomical models of two adults and two children for dosimetric simulations. Phys Med Biol. 2010; 55(2):N23–N38. [PubMed: 20019402]
12. Hasgall PADGF, Baumgartner C, Neufeld E, Gosselin MC, Payne D, Klingenböck A, Kuster N. IT'IS Database for thermal and electromagnetic parameters of biological tissues. Version 3.0. 2015 Sep 1.
13. Carluccio G, Erricolo D, Oh S, Collins CM. An Approach to Rapid Calculation of Temperature Change in Tissue Using Spatial Filters to Approximate Effects of Thermal Conduction. Ieee T Bio-Med Eng. 2013; 60(6):1735–1741.

14. Eichfelder G, Gebhardt M. Local Specific Absorption Rate Control for Parallel Transmission by Virtual Observation Points. Magnet Reson Med. 2011; 66(5):1468–1476.
15. Hart HR, Bottomley PA, Edelstein WA, Karr SG, Leue WM, Mueller O, Redington RW, Schenck JF, Smith LS, Vatis D. Nuclear Magnetic-Resonance Imaging - Contrast-to-Noise Ratio as a Function of Strength of Magnetic-Field. Am J Roentgenol. 1983; 141(6):1195–1201. [PubMed: 6606316]
16. Zhang Z, Yip CY, Grissom W, Noll DC, Boada FE, Stenger VA. Reduction of transmitter B1 inhomogeneity with transmit SENSE slice-select pulses. Magn Reson Med. 2007; 57(5):842–847. [PubMed: 17457863]
17. Grissom W, Yip CY, Zhang Z, Stenger VA, Fessler JA, Noll DC. Spatial domain method for the design of RF pulses in multicoil parallel excitation. Magnetic Resonance in Medicine. 2006; 56(3): 620–629. [PubMed: 16894579]
18. Hoyos-Idrobo A, Weiss P, Massire A, Amadon A, Boulant N. On Variant Strategies to Solve the Magnitude Least Squares Optimization Problem in Parallel Transmission Pulse Design and Under Strict SAR and Power Constraints. Ieee T Med Imaging. 2014; 33(3):739–748.
19. Guerin B, Gebhardt M, Cauley S, Adalsteinsson E, Wald LL. Local specific absorption rate (SAR), global SAR, transmitter power, and excitation accuracy trade-offs in low flip-angle parallel transmit pulse design. Magn Reson Med. 2014; 71(4):1446–1457. [PubMed: 23776100]
20. Setsompop K, Wald LL, Alagappan V, Gagoski BA, Adalsteinsson E. Magnitude least squares optimization for parallel radio frequency excitation design demonstrated at 7 Tesla with eight channels. Magn Reson Med. 2008; 59(4):908–915. [PubMed: 18383281]
21. Dupas L, Massire A, Amadon A, Vignaud A, Boulant N. Two-spoke placement optimization under explicit specific absorption rate and power constraints in parallel transmission at ultra-high field. J Magn Reson. 2015; 255:59–67. [PubMed: 25912342]
22. Cloos MA, Boulant N, Luong M, Ferrand G, Giacomini E, Le Bihan D, Amadon A. kT -points: short three-dimensional tailored RF pulses for flip-angle homogenization over an extended volume. Magn Reson Med. 2012; 67(1):72–80. [PubMed: 21590724]
23. Erturk MA, Tian J, Van de Moortele PF, Adriany G, Metzger GJ. Development and evaluation of a multichannel endorectal RF coil for prostate MRI at 7.0T in combination with an external surface array. J Magn Reson Imaging. 2016; 43(6):1279–1287. [PubMed: 26584144]
24. Yarnykh VL. Actual flip-angle imaging in the pulsed steady state: a method for rapid three-dimensional mapping of the transmitted radiofrequency field. Magn Reson Med. 2007; 57(1):192–200. [PubMed: 17191242]
25. Edelstein WA, Glover GH, Hardy CJ, Redington RW. The Intrinsic Signal-to-Noise Ratio in Nmr Imaging. Magnet Reson Med. 1986; 3(4):604–618.
26. Metzger GJ, Snyder C, Akgun C, Vaughan T, Ugurbil K, Van de Moortele PF. Local B1+ shimming for prostate imaging with transceiver arrays at 7.0T based on subject-dependent transmit phase measurements. Magnetic Resonance in Medicine. 2008; 59(2):396–409. [PubMed: 18228604]
27. Adriany G, Gozubuyuk A, Auerbach EJ, Van de Moortele PF, Andersen P, Vaughan JT, Ugurbil K. A 32 channel Transmit/Receive Transmission Line Head Array for 3D RF Shimming. Proc Int Soc Magn Reson Med Sci Meet Exhib Int Soc Magn Reson Med Sci Meet Exhib. 2007; 2007:166.
28. Gilbert KM, Curtis AT, Gati JS, Klassen LM, Menon RS. A radiofrequency coil to facilitate B(1) (+) shimming and parallel imaging acceleration in three dimensions at 7 T. NMR Biomed. 2011; 24(7):815–823. [PubMed: 21834005]
29. Kozlov, M.; Turner, R. RF transmit performance comparison for several MRI head array geometries; Eur Microw Conf; 2013. p. 601-604.
30. Wu X, Tian J, Schmitter S, Vaughan JT, Ugurbil K, Van de Moortele PF. Distributing coil elements in three dimensions enhances parallel transmission multiband RF performance: A simulation study in the human brain at 7 Tesla. Magn Reson Med. 2016; 75(6):2464–2472. [PubMed: 26997332]
31. Winter L, Niendorf T. Electrodynamics and radiofrequency antenna concepts for human magnetic resonance at 23.5 T (1 GHz) and beyond. MAGMA. 2016
32. Wiesinger F, Boesiger P, Pruessmann KP. Electrodynamics and ultimate SNR in parallel MR imaging. Magn Reson Med. 2004; 52(2):376–390. [PubMed: 15282821]

33. Wiggins, GC.; Lakshmanan, K.; Chen, G. The Distributed Inductance Electric Dipole Antenna. International Society of Magnetic Resonance in Medicine 23rd Annual Meeting & Exhibition; Toronto, Canada. 2015. p. 3100
34. Steensma, B.; Andrade, AVO.; Klomp, DW.; Van den Berg, CA.; Luijten, PR.; Raaijmakers, AJ. Body imaging at 7 Tesla with much lower SAR levels: an introduction of the Snake Antenna array. International Society of Magnetic Resonance in Medicine 23rd Annual Meeting & Exhibition; Singapore. 2016. p. 0395
35. Erturk MA, Raaijmakers AJ, Adriany G, Ugurbil K, Metzger GJ. A 16-channel combined loop-dipole transceiver array for 7 Tesla body MRI. Magn Reson Med. 2016
36. Chen, G.; Lattanzi, R.; Sodickson, DK.; Wiggins, GC. Approaching the Ultimate Intrinsic SNR with Dense Arrays of Electric Dipole Antennas. International Society of Magnetic Resonance in Medicine 23rd Annual Meeting & Exhibition; International Society of Magnetic Resonance in Medicine 23rd Annual Meeting & Exhibition; Singapore. 2016. p. 0168
37. Hoult DI, Lauterbur PC. Sensitivity of the Zeugmatographic Experiment Involving Human Samples. Journal of Magnetic Resonance. 1979; 34(2):425–433.
38. Hoult DI, Phil D. Sensitivity and power deposition in a high-field imaging experiment. J Magn Reson Imaging. 2000; 12(1):46–67. [PubMed: 10931564]
39. Lattanzi R, Sodickson DK, Grant AK, Zhu Y. Electrodynamic constraints on homogeneity and radiofrequency power deposition in multiple coil excitations. Magn Reson Med. 2009; 61(2):315–334. [PubMed: 19165885]
40. El-Sharkawy AM, Qian D, Bottomley PA. The performance of interventional loopless MRI antennae at higher magnetic field strengths. Med Phys. 2008; 35(5):1995–2006. [PubMed: 18561676]
41. Erturk MA, El-Sharkawy AM, Bottomley PA. Interventional loopless antenna at 7 T. Magn Reson Med. 2012; 68(3):980–988. [PubMed: 22161992]
42. Pohmann R, Speck O, Scheffler K. Signal-to-noise ratio and MR tissue parameters in human brain imaging at 3, 7, and 9.4 tesla using current receive coil arrays. Magn Reson Med. 2016; 75(2): 801–809. [PubMed: 25820458]
43. van den Bergen B, van den Berg CA, Klomp DW, Lagendijk JJ. SAR and power implications of different RF shimming strategies in the pelvis for 7.0T MRI. J Magn Reson Imaging. 2009; 30(1): 194–202. [PubMed: 19557737]
44. Deniz CM, Brown R, Lattanzi R, Alon L, Sodickson DK, Zhu Y. Maximum efficiency radiofrequency shimming: Theory and initial application for hip imaging at 7 tesla. Magn Reson Med. 2013; 69(5):1379–1388. [PubMed: 22714835]
45. Metzger GJ, Auerbach EJ, Akgun C, Simonson J, Bi X, Ugurbil K, van de Moortele PF. Dynamically applied B1+ shimming solutions for non-contrast enhanced renal angiography at 7.0 Tesla. Magn Reson Med. 2013; 69(1):114–126. [PubMed: 22442056]
46. Orzada S, Maderwald S, Poser BA, Bitz AK, Quick HH, Ladd ME. RF excitation using time interleaved acquisition of modes (TIAMO) to address B1 inhomogeneity in high-field MRI. Magn Reson Med. 2010; 64(2):327–333. [PubMed: 20574991]
47. Zelinski AC, Wald LL, Setsompop K, Alagappan V, Gagoski BA, Goyal VK, Adalsteinsson E. Fast slice-selective radio-frequency excitation pulses for mitigating B+1 inhomogeneity in the human brain at 7 Tesla. Magn Reson Med. 2008; 59(6):1355–1364. [PubMed: 18506800]
48. Grissom WA, Xu D, Kerr AB, Fessler JA, Noll DC. Fast large-tip-angle multidimensional and parallel RF pulse design in MRI. IEEE Trans Med Imaging. 2009; 28(10):1548–1559. [PubMed: 19447704]
49. Moore J, Jankiewicz M, Anderson AW, Gore JC. Slice-selective excitation with B(1)(+)-insensitive composite pulses. J Magn Reson. 2012; 214(1):200–211. [PubMed: 22177383]
50. Boulant N, Massire A, Amadon A, Vignaud A. Radiofrequency pulse design in parallel transmission under strict temperature constraints. Magn Reson Med. 2014; 72(3):679–688. [PubMed: 24155266]
51. Guerin B, Setsompop K, Ye H, Poser BA, Stenger AV, Wald LL. Design of parallel transmission pulses for simultaneous multislice with explicit control for peak power and local specific absorption rate. Magn Reson Med. 2015; 73(5):1946–1953. [PubMed: 24938991]

52. Gras V, Vignaud A, Amadon A, Le Bihan D, Boulant N. Universal pulses: A new concept for calibration-free parallel transmission. Magn Reson Med. 2016
53. Massire A, Vignaud A, Robert B, Le Bihan D, Boulant N, Amadon A. Parallel-transmission-enabled three-dimensional T2 -weighted imaging of the human brain at 7 Tesla. Magn Reson Med. 2015; 73(6):2195–2203. [PubMed: 25046558]
54. Eggenschwiler F, O'Brien KR, Gruetter R, Marques JP. Improving T2 -weighted imaging at high field through the use of kT -points. Magn Reson Med. 2014; 71(4):1478–1488. [PubMed: 23788025]
55. Malik SJ, Beqiri A, Padormo F, Hajnal JV. Direct signal control of the steady-state response of 3D-FSE sequences. Magn Reson Med. 2015; 73(3):951–963. [PubMed: 24639096]
56. Cloos MA, Knoll F, Zhao T, Block KT, Bruno M, Wiggins GC, Sodickson DK. Multiparametric imaging with heterogeneous radiofrequency fields. Nat Commun. 2016; 7:12445. [PubMed: 27526996]
57. Murbach M, Neufeld E, Cabot E, Zastrow E, Corcoles J, Kainz W, Kuster N. Virtual population-based assessment of the impact of 3 Tesla radiofrequency shimming and thermoregulation on safety and B + uniformity. Magn Reson Med. 2015
58. Deniz CM, Alon L, Brown R, Zhu Y. Subject- and resource-specific monitoring and proactive management of parallel radiofrequency transmission. Magn Reson Med. 2015
59. Boulant N, Wu X, Adriany G, Schmitter S, Ugurbil K, Van de Moortele PF. Direct control of the temperature rise in parallel transmission by means of temperature virtual observation points: Simulations at 10.5 Tesla. Magn Reson Med. 2016; 75(1):249–256. [PubMed: 25754685]
60. Kuehne A, Goluch S, Waxmann P, Seifert F, Ittermann B, Moser E, Laistler E. Power Balance and Loss Mechanism Analysis in RF Transmit Coil Arrays. Magnet Reson Med. 2015; 74(4):1165–1176.
61. Erturk MA, El-Sharkawy AM, Bottomley PA. Monitoring local heating around an interventional MRI antenna with RF radiometry. Med Phys. 2015; 42(3):1411–1423. [PubMed: 25735295]
62. Shrivastava D, Hanson T, Kulesa J, Tian J, Adriany G, Vaughan JT. Radiofrequency heating in porcine models with a "large" 32 cm internal diameter, 7 T (296 MHz) head coil. Magn Reson Med. 2011; 66(1):255–263. [PubMed: 21337423]
63. Shrivastava D, Utecht L, Tian J, Hughes J, Vaughan JT. In vivo radiofrequency heating in swine in a 3T (123.2-MHz) birdcage whole body coil. Magn Reson Med. 2014; 72(4):1141–1150. [PubMed: 24259413]
64. Simonis F, Raaijmakers A, Lagendijk J, van den Berg C. Validating subject-specific RF and thermal simulations in the calf muscle using MR-based temperature measurements. Magn Reson Med. 2016

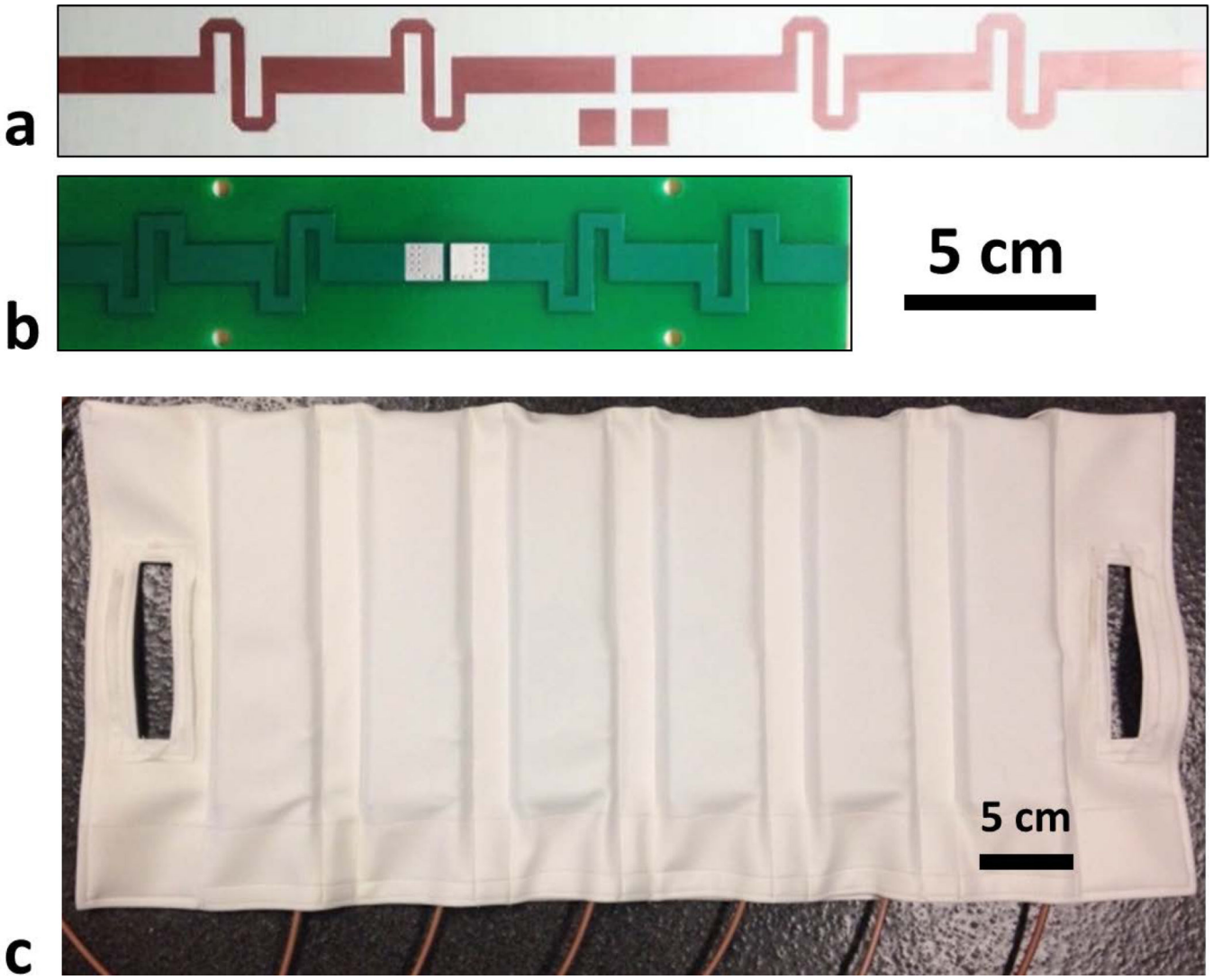

Figure 1.
(a) Dipole antenna elements at 7.0 T and (b) 10.5 T. (c) Anterior housing of the dipole antenna array containing six elements.

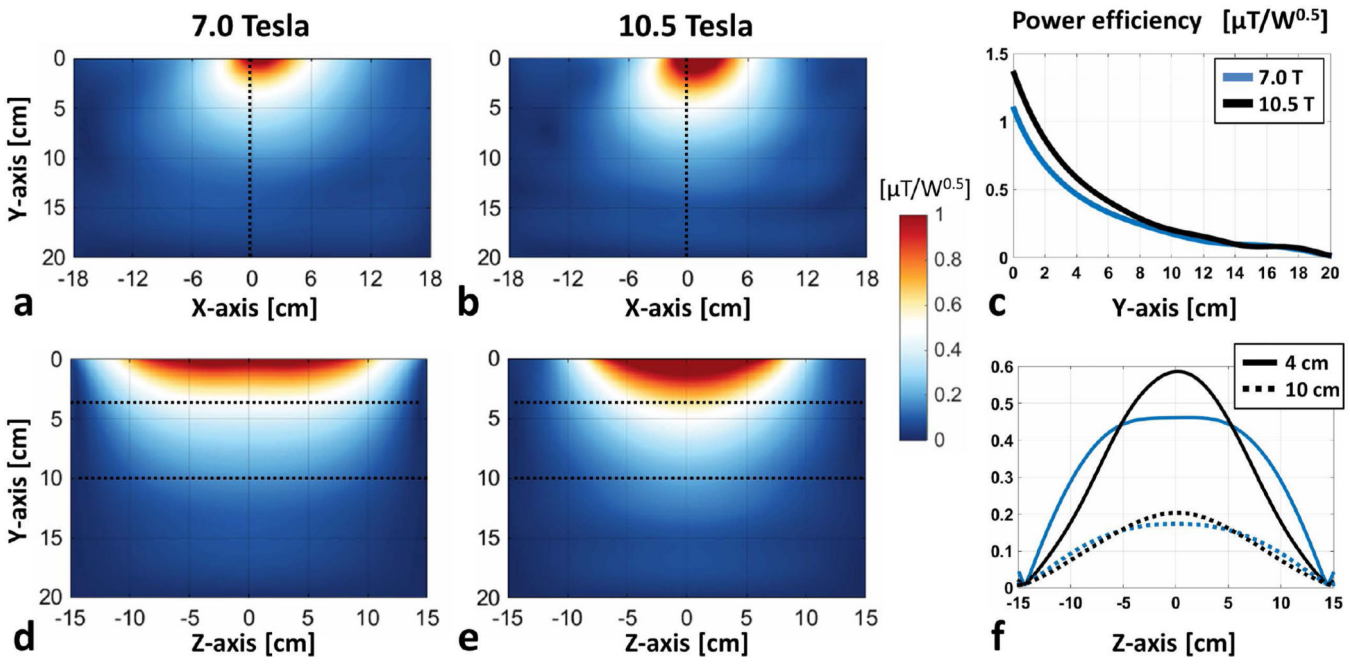

Figure 2.

(a) Power efficiency distributions of 7.0 T and (b) 10.5 T dipole antenna elements along axial slices inside a uniform phantom are shown. (c) Power efficiency profiles along the center of the axial slices are plotted (blue: 7.0 T, black: 10.5 T). Power efficiency distributions of 7.0 and 10.5 T antennae inside sagittal slices are shown in (d) and (e), respectively. (f) Power efficiency profiles at a depth of 4 cm (solid) and 10 cm (dashed) are plotted for the 7.0 and 10.5 T antennae in blue and black, respectively.

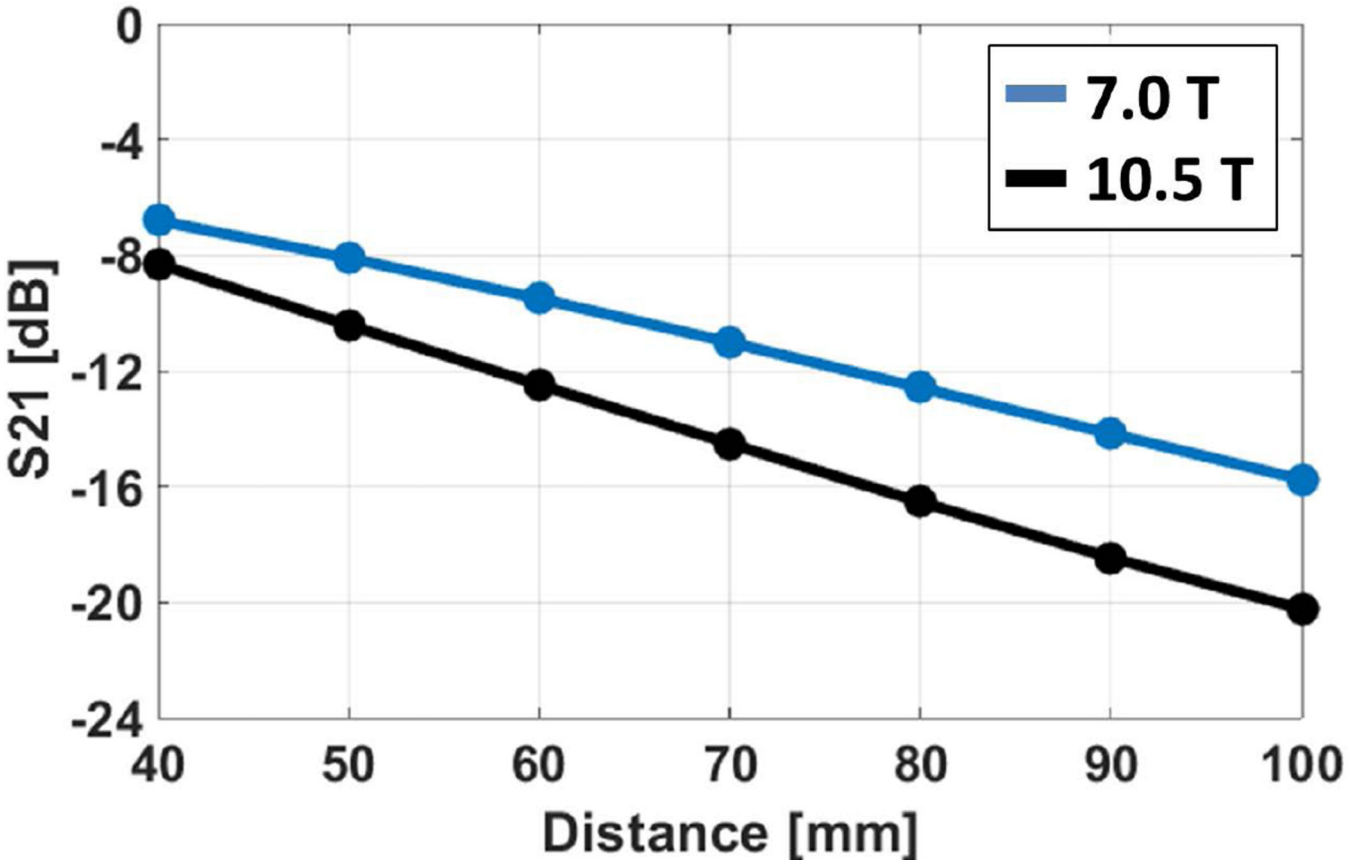

Figure 3.

Amount of coupling (in dB) between neighboring antenna elements placed on a rectangular uniform phantom are plotted against their center-to-center separation distances (blue: 7.0 T, and black: 10.5 T antenna elements).

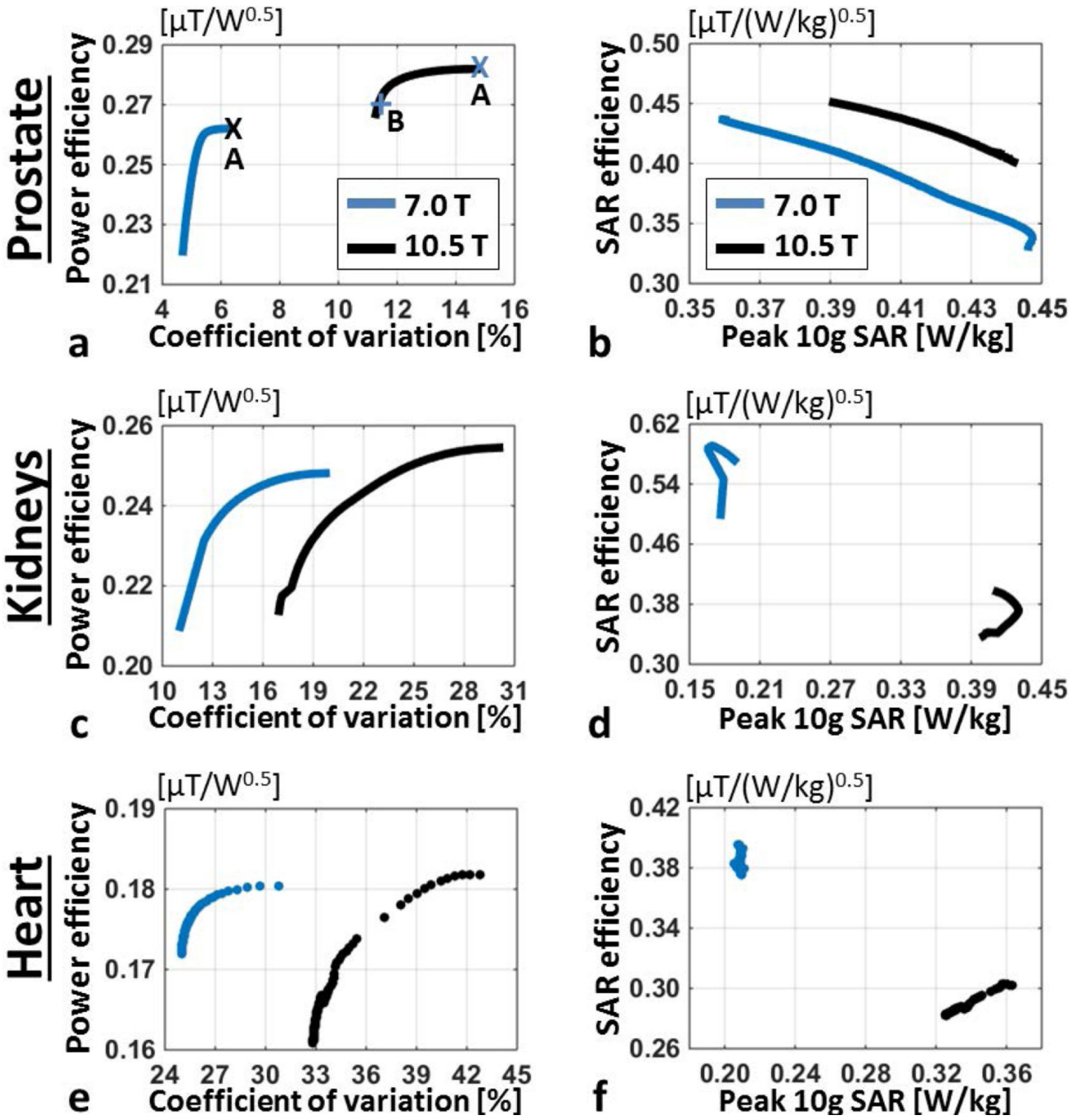

Figure 4.

(a) Power efficiency vs coefficient of variation of B1+ magnitude inside the prostate of Duke and (b) SAR efficiency vs peak 10g local SAR are shown for 7.0 T (blue) and 10.5 T (black) antenna arrays. Power efficiency distributions pertaining to annotated shim solutions are shown in Supporting Figure S1. (c) Average power efficiency vs its coefficient of variation inside kidneys and (e) heart are plotted. (d) SAR efficiency vs peak 10g local SAR plots for kidney and (f) heart phase-only shim solutions are displayed.

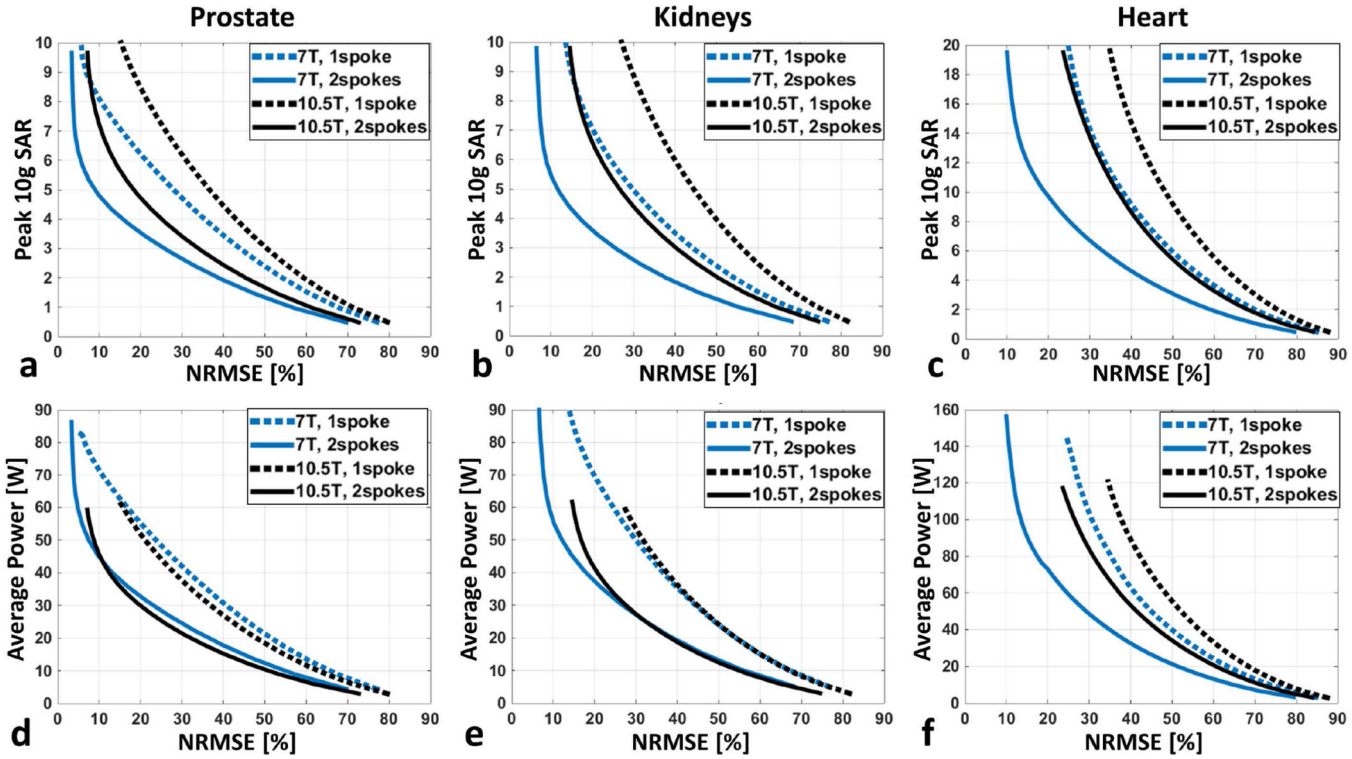

Figure 5.

L-curves demonstrating the tradeoff between excitation error (NRMSE) and resulting peak local SAR for 7.0 T (blue) and 10.5 T (black) arrays when designing 1-spoke (dashed) and 2-spoke (solid) pTx pulses to image (a) the prostate, (b) the kidneys and (c) the heart. The pTx pulses were designed with explicit local SAR constraint, and the L-curve per design scenario was created by varying the predefined peak 10 g SAR limit. In all cases, the nominal flip angle was 45 degrees. Note that combining 2-spoke pulse design with our 10.5T dipole array provided comparable (when imaging kidneys or heart) or even better (when imaging prostate) RF performance than single-spoke designs at 7.0T. L-curves demonstrating the tradeoff between excitation error (NRMSE) and required average total array power for 7.0 T (blue) and 10.5 T (black) arrays for 1- and 2-spoke (solid) pTx pulses to image (d) the prostate, (e) the kidneys and (f) the heart are shown.

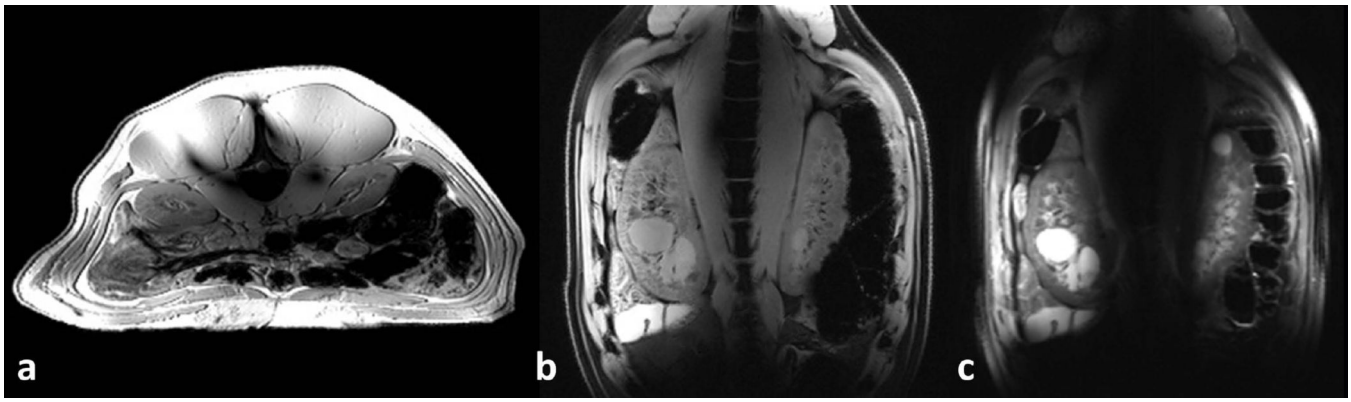

Figure 6.

(a) Axial and (b) coronal GRE images acquired inside the abdomen of a swine with anterior-posterior dimension of 19 cm. Phase-only RF shimming inside the kidneys are used in acquisitions. (c) Coronal FSE image demonstrates good contrast between the cysts inside the kidneys, cortex and medulla. Image quality in the middle of the imaging slice is hampered due to B1+ dropoff.

Table 1

Mean values of numerically computed receive B_1^- performance of antenna arrays inside the prostate, kidneys and heart are listed (distributions are shown in Supporting Figure S2). Anticipated relative SNR gains at 10.5 T compared to 7.0 T are calculated using Eq. [1] and listed along the last column.

	RSOS B_1^- combination [$\mu T/W^{0.5}$]		Relative SNR gain of the 10.5 T antenna array vs the 7.0 T array
	Antenna array at 7.0 T	Antenna array at 10.5 T	
Prostate	0.279	0.296	2.39
Kidneys	0.353	0.365	2.33
Heart	0.297	0.283	2.14